

Laboratory validation of a new hydro-mechanical energy-based brittleness index model for hydraulic fracturing

Runhua Feng^{a*}, Joel Sarout^b, Jeremie Dautriat^b, Yousef M Al Ghuwainim^{a,c}, Reza Rezaee^a,
Mohammad Sarmadivaleh^{a*}

^aSchool of WASM: Minerals, Energy and Chemical Engineering, Curtin University, 26 Dick Perry Ave, Kensington, WA 6151 Australia

^bCSIRO Energy, Kensington, WA 6152, Australia

^cDepartment of Petroleum Engineering and Geosciences (CPG), King Fahd University of Petroleum & Minerals, KFUPM, Dhahran 31261, Saudi Arabia

*Corresponding author:

E-mail address: runhua.feng@student.curtin.edu.au (R.Feng);

mohammad.sarmadivaleh@curtin.edu.au (M.sarmadivaleh)

Highlights

- A new brittleness index (BI) model based on quantification of the non-seismic deformation energy (E_d) induced by hydraulic fracturing is proposed and experimentally validated.
- Hydraulic fracturing tests are conducted on different types of synthetic rocks under true triaxial stress conditions, either $\sigma_v = 6.5$ MPa, $\sigma_H = 3$ MPa, $\sigma_h = 1.5$ MPa or $\sigma_v = 15$ MPa, $\sigma_H = 10$ MPa, $\sigma_h = 5$ MPa.
- The existing BI models, (i) based on sonic and density logs from Rickman et al (2008), and (ii) based on Mohr-Coulomb's criteria from Papanastasiou et al (2016) are compared with our model.

Abstract

Brittleness Index (BI) is a critical parameter characterising the deformation regime of geo-materials, covering the range from purely brittle (fractures) to ductile (plastic flow). A variety of BI models have been developed based on rock properties such as mineralogy, elastic parameters, or stress-strain data. However, very few of them are based on the deformation induced by hydro-mechanical interactions emerging in a wide range of underground engineering applications. In this study, we develop a BI model based on the partitioning of the injection energy E_I into non-seismic deformation energy E_d associated with hydraulic fracture propagation. To calculate the E_d , we apply a model for temporal fracturing area (A_d) within the penny-shaped fracture; we also correlate the wellbore pressure and the three-dimensional strain induced by hydraulic fracturing of the different types of rock samples subjected to true triaxial stress conditions (TTSC), either $\sigma_v = 6.5$ MPa, $\sigma_H = 3$ MPa, $\sigma_h = 1.5$ MPa or $\sigma_v = 15$ MPa, $\sigma_H = 10$ MPa, $\sigma_h = 5$ MPa for all tests. As a comparison, the BI is also quantified based on the existing models: (i) acoustic measurement from Rickman et al (2008), and (ii) the Mohr-Coulomb's criteria from Papanastasiou et al (2016). The non-seismic deformation energy E_d ranges between 32.4% and 90.6% of the total injection energy E_I , which is slightly higher than reported from field-scale data (15% to 80%), and is comparable to other laboratory-derived data (18% to 94%). The results show that the predictions based on our newly proposed hydro-mechanical energy-based BI model are qualitatively consistent with Papanastasiou et al.'s, but less so with Rickman et al.'s. Our BI model is shown to be stress-dependent and capable of capturing the brittle-to-ductile behaviour within a wide range of rheological samples subjected to hydraulic fracturing. This study demonstrates that our BI model opens a new way for quantifying the brittleness index regarding to realistic propagation scenarios, showing its superior robustness for such underground applications.

Keywords: Brittleness index model; Hydraulic fracturing; Hydro-mechanical deformation energy; Temporal fracturing area; Three-dimensional strain

1. Introduction

Brittleness Index (BI) has been recognized as one of the key parameters controlling fracture development in geo-materials during reservoir stimulation,¹⁻⁵ fluid-induced seismicity,⁶⁻⁸ and magma migration.⁹ However, the definition and quantification of a reliable BI for hydro-mechanical applications remains a challenge, i.e., the existing BI models are mainly based on rock mechanical parameters but neglect the coupled hydro-mechanical interactions associated with rock deformation at depth. A better understanding of the hydro-mechanical deformation in geo-materials can facilitate not only theoretical modelling and the BI model development, but also provide critical insights for field applications.

The deformation of a geo-material comprises several stages with shear stress increasing toward failure: Stage I – low-strain initial elastic deformation; Stage II – non-recoverable (inelastic) deformation, e.g., brittle micro-cracking, or ductile/plastic flow; Stage III – micro-cracks coalescence and macroscopic fracture propagation/strain localisation, resulting in the failure of the rock. In this context, conventional BI models were developed based on either a) triaxial stress-strain data; b) the recoverable/total strain energy ratio; or c) mechanical parameters derived from multiple rock mechanics tests.¹⁰⁻¹² Such BI models are suitable for near-surface applications with relatively low magnitudes of deviatoric stress, e.g., tunnel engineering.¹³⁻¹⁵ However, they may have limited application in deeper underground environments where natural or anthropogenic fluid-driven fracturing takes place. The depth, and therefore the in situ effective (triaxial) stress will affect the mechanical response of the rock, e.g., static and dynamic elastic properties, brittleness/ductility, yield/failure type, post-failure behaviour.^{4,5,16-23} Such depth-dependent rock deformation features should be accounted for in order to devise the most reliable and efficient BI model, i.e., sensitive, discriminative, reproducible.

Rickman et al.²⁴ proposed a practical BI model for unconventional shale reservoirs based on sonic and density logs, which provides the dynamic Young's Modulus E_{dyn} , and Poisson's ratio ν_{dyn} but disregards the post-failure response of the rock, which limits the applicability of this model to relative brittleness quantification only.²⁵ Feng et al.³ showed that Rickman et al.'s BI model agrees only qualitatively with other models based on the post-failure behaviour of the rock. Reported limitations of this BI model include: (i) unphysical increase of the BI with confining pressure;²⁶ and (ii) limited discrimination between brittle and ductile depth intervals.^{27,28} Despite its reported limitations, this BI model is commonly applied in the field. More recently, Papanastasiou et al.²⁹ proposed an analytical BI based on Mohr-Coulomb's

brittle failure model, where the internal friction angle ϕ , the cohesion C_o , the maximum (σ_{\max} vertical) and minimum (σ_{\min} horizontal) principal stresses are accounted for in a mode-I hydraulic fracture propagation scenario. However, the BI values computed with this model are unexpectedly low when the difference between the maximum (σ_{\max}) and minimum stress (σ_{\min}) becomes significant.³

An alternative BI model based on hydraulic fracturing energy was recently reported by Feng et al.³, in which the energy ratio between deformation energy E_d and injection energy E_I is estimated from the wellbore pressure data, lacking of the direct strain measurements. They also experimentally examined the consistency and applicability of a total of eight distinct BI models available in the literature, including the abovementioned BI models³. Their results indicated that the models from Rickman et al.²⁴, Papanastasiou et al.²⁹, and Feng et al.³ followed qualitatively consistent trends for the tested rock types. However, the magnitude of the BI from Rickman et al.²⁴ was larger than the one from seven other BI models analysed in [3]. Feng et al.³ also showed that the BI values from Papanastasiou et al.²⁹ range between 0.1 and 0.22 (under the stress conditions of $\sigma_v = 8\text{MPa}$, $\sigma_H = 8\text{MPa}$, $\sigma_h = 0\text{MPa}$), which is significantly lower than the BI value quantified from seven other BI models. These discrepancies are worthily to be further investigated, especially for variable stress conditions.

Beyond the injection rate, the hydraulic fracture initiation and propagation in geomaterials is governed by multiple parameters, including, but not limited to (i) the property of injected fluid; (ii) rock mechanical properties (elastic moduli, brittleness/ductility, mechanical strength, fracture toughness); and (iii) stress state at depth^{3,4,30-35}. These studies reveal that for assessing the hydraulic fracturing performance the BI evaluation based on the multiple parameters is challenging. In addition, the availability/variability of these parameters may lead to more uncertainties of the BI for the field study. To our knowledge, no BI model based on hydraulic fracturing-induced deformation subjected to true triaxial stress conditions has been published in the literature.

The efforts/novelty of research in this paper mainly involves: **(i)** A new hydro-mechanical energy-based BI model based on the direct quantification of both injection energy E_I and non-seismic deformation energy E_d for the materials subjected to hydraulic fracturing is introduced (Section 2.2); and its applicability is demonstrated (Sections 5). **(ii)** A rich set of new hydraulic fracturing data from 25 cubic rock specimens (plus two PMMAs) subjected to true triaxial stress conditions at laboratory (same stress conditions either $\sigma_v = 6.5\text{MPa}$, $\sigma_H = 3\text{MPa}$, $\sigma_h = 1.5\text{MPa}$ or $\sigma_v = 15\text{MPa}$, $\sigma_H = 10\text{MPa}$, $\sigma_h = 5\text{MPa}$ for all tests) are reported (Section 3); the

correlation between the wellbore pressure and 3D strains are proposed (Section 4.1). The mechanical characterisation of the various rock types studied here is reported in Appendix B and involved a total of 10 UCS and 15 triaxial tests on cylindrical plugs. **(iii)** The results of the new and existing BI models are compared in light of these data, and the consistency between them, as well as their validity and applicability are discussed (Sections 4 and 5).

2. The Brittleness Index

2.1 Existing Brittleness Index (BI) models

Feng et al.³ recently discussed the consistency and applicability of eight published BI models, and demonstrated that the BI models based on petrophysical logs,²⁴ or on Mohr-Coulomb's failure criterion²⁹ were qualitatively consistent with Feng et al.'s energy-based BI model for multiple rock types.³ However, they observed significant discrepancies in terms of the BI values each model predicts for those rocks, with Rickman et al.²⁴'s BI values being too large, and Papanastasiou et al.²⁹'s BI values being too low compared to Feng et al.³'s. As they seem to yield extreme values of BI for a wide range of rock types, these two models will be used in this study for quantification and comparison, i.e.,

$$BI_1 = \frac{1}{2} \left(\frac{E_{dyn}^{(0.8-\phi)-1}}{8-1} + \frac{v_{dyn}^{-0.4}}{0.15-0.4} \right), \quad (1)$$

$$BI_2 = 1 - \frac{(\sigma_1 - \sigma_3)}{2 C_o \cos \Phi + (\sigma_1 + \sigma_3) \sin \Phi}, \quad (2)$$

where E_{dyn} is the dynamic Young's Modulus and v_{dyn} is Poisson's ratio determined either from sonic/density logs, or ultrasonic wave velocity measurements in the lab; ϕ is the porosity; σ_1 and σ_3 are the maximum and minimum principal stresses, respectively; Φ and C_o are Mohr-Coulomb's internal friction angle and cohesion parameters, respectively.

2.2 New hydro-mechanical energy-based Brittleness Index model

2.2.1 Model definition

At a given temperature, the mechanical failure of single crystals is essentially driven by either brittle fracturing or ductile/plastic flow.³⁶ However, in poly-crystalline mineral aggregates constituting sedimentary or metamorphic rocks, both failure modes coexist (semi-brittle fracturing), and their relative importance is governed by the magnitude of the prevailing mean effective stress or depth³⁷⁻³⁹. During hydraulic fracturing of polycrystalline rocks, the supplied injection energy E_I is partitioned into a) non-seismic deformation energy E_d , i.e., fracture tip

resistance and separation energy necessary to overcome cohesive forces; b) kinetic energy E_k associated with crack propagation (create new fracture surface area); and c) radiated seismic energy E_r . The latter term (E_r) can conveniently be neglected in the energy balance, i.e., $E_r \ll E_d$ and $E_r \ll E_k$ ⁴⁰⁻⁴². The supplied energy- injection energy E_I from pump can conveniently be written as^{40,41}

$$E_I = Q \int_{t_i}^{t_e} P(t) dt, \quad (3)$$

where Q is the constant injection rate, $P(t)$ is the wellbore pressure during the injection period, t is time, t_i is the time of hydraulic fracture initiation, and t_e is the time of propagation end. Considering the displacement induced by the opening hydraulic fracture (2D displacement field), the induced non-seismic deformation energy E_d reads

$$E_d = \int_{w_i}^{w_e} A_d P(w) dw, \quad (4)$$

where A_d is the temporal-evolving fracturing area (surface roughness is neglected); w is the width(displacement) resulting from the opening fracture; $P(w)$ is the wellbore pressure corresponding to the displacement w , from fracture nucleation w_i , to the end of fracture propagation w_e . In an ideally ductile rock, most of the injection energy E_I is dissipated through non-seismic deformation ($E_I \sim E_d$), while kinetic energy E_k can be neglected, i.e., $E_k \ll E_d$ ³. The opposite holds in a brittle rock, for which $E_I \sim E_k$ and $E_d \ll E_k$. In this context, we defined a new Brittleness Index BI_3 as the ratio of E_d/E_I ,

$$BI_3 = 1 - \frac{E_d}{E_I} = 1 - \frac{\int_{w_i}^{w_e} A_d P(w) dw}{Q \int_{t_1}^{t_2} P(t) dt}. \quad (5)$$

In practice, fracture propagation in controlled laboratory conditions can be complex, e.g., jagged or straight propagation, orthogonal to the minimum principal stress or not. In this study, we consider both: the fracture propagates perpendicular to the direction of minimum stress (e.g., horizontal stress σ_h); and the fracture ends up inclined with respect to both directions (e.g., horizontal stress σ_h and σ_H) (**Fig.1a**).

2.2.2 Model parametrisation

Considering a single vertical fracture subjected to the *in-situ* horizontal stresses σ_h and σ_H , (see **Fig.1a**), the resulting normal stress on the fracture's walls σ_w reads

$$\sigma_F = \sigma_h \cos \theta + \sigma_H \sin \theta, \quad (6)$$

where θ is the angle between the fracture plane and the maximum horizontal stress σ_H (or between the fracture's normal vector and the minimum horizontal stress σ_h). The resulting fracture width (w) in this plane reads

$$w = \varepsilon_h L_h \cos \theta + \varepsilon_H L_H \sin \theta, \quad (7)$$

where ε_h and ε_H are the strains induced by the fracture in the two horizontal directions, i.e., along σ_h and σ_H , respectively; while L_h and L_H are the dimensions of the sample in these directions, respectively. In the case of a fracture orientation where $\theta = 0^\circ$, the normal stress σ_w reduces to σ_h , and w reduces to $\varepsilon_h \times L_h$.

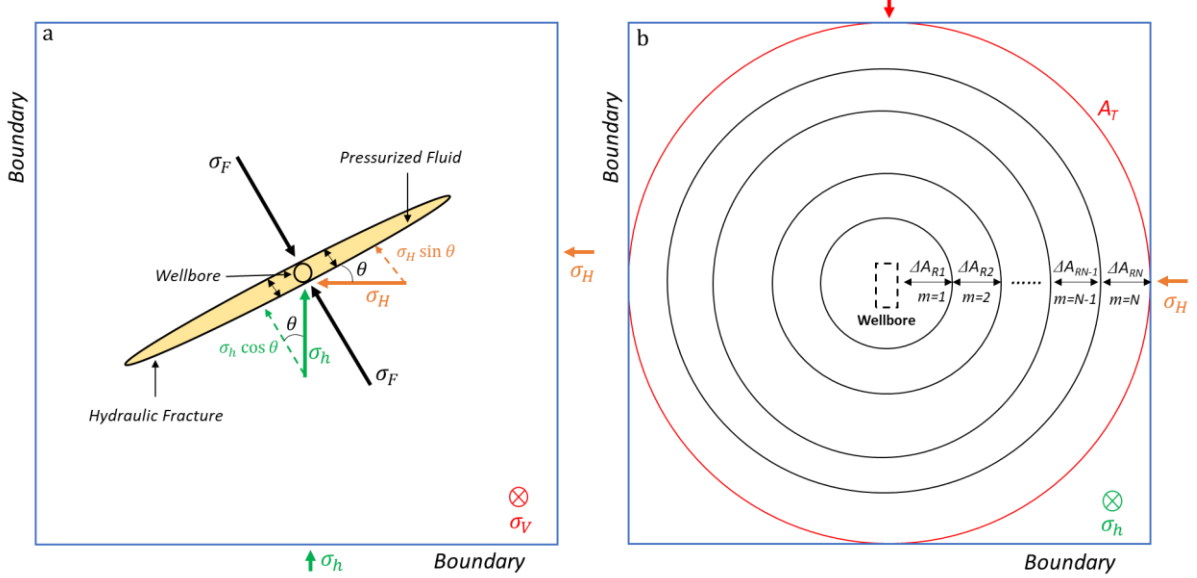


Fig.1 (a) 2D Schematic of an inclined hydraulic fracture propagation; (b) 2D schematic of the homothetic growth of a penny-shaped fracture, outlining the temporal fracturing area A_d .

Poiseuille's law is used to describe the flow of Newtonian fluids driven by fluid pressure within a penny-shaped fracture, ^{43,44} we consider a possible fluid lag often observed in laboratory experiments ⁴⁴⁻⁴⁶, i.e., the fluid radius (R_f) is smaller to the fracture radius (R), $R_f < R$, reads

$$q(r, t) = w(r, t) u(r, t) = -\frac{w(r, t)^3}{12 \mu_f} \frac{\partial p_f(r, t)}{\partial r}, \text{ with } 0 < r < R_f < R, \quad (8)$$

where $q(r, t)$ is the flow rate per unit of fracture perimeter; $w(r, t)$ is the width/aperture of the fracture; p_f is the fluid pressure within the fracture; $u(t) = dR_f(t)/dt$ is the velocity of the fluid at the fluid front $r = R_f(t)$; and μ_f is the viscosity of the fluid. Note that $R_f = R_f(t)$ and $R = R(t)$ are time-dependent during fracture propagation.

With the mathematic transformation (detailed in Feng et al.⁴⁷), the analytical model for the fracturing area A_d denoted in **Eqs.4 and 5** is proposed and validated by in [47], i.e.,

$$A_d = \sum_{m=1}^n (\Delta A_R)_m \cong A_T \frac{\sum_{m=1}^n \left(\sqrt{-\frac{w_m^2}{12 \mu_f} \left(\frac{\Delta P}{\Delta t} \right)_m} \right)}{\sum_{i=1}^N \left(\sqrt{-\frac{w_i^2}{12 \mu_f} \left(\frac{\Delta P}{\Delta t} \right)_i} \right)}, \text{ with } 1 \leq i \leq N \text{ and } 1 \leq m \leq n \leq N \quad (9)$$

Where the indices i and m reflect the time steps between the nucleation ($i = m = 1$), and the end of propagation ($i = m = N$) of the hydraulic fracture, i.e., when it reaches the boundaries of the

rock sample. $(\Delta A_R)_m$ is a small enough incremental increase in fracture surface area per time increment Δt_m ; A_T is the total (maximum) fractured area; w_m is the width (aperture) of fracture at the time step m ; P is the wellbore pressure monitored per time increment Δt_m during the period from fracture initiation to the end of propagation.

3. Hydraulic fracturing experiments

Hydraulic fracturing experiments under true triaxial stress conditions were conducted on a suite of synthetic rocks (dimension of 50x50x50mm, see the details of sample preparation and rock characterisation in **Appendix B**) in order to evaluate the validity and performance of the new hydro-mechanical energy-based Brittleness Index model BI_3 (**Eq.5**), which entails validating the fracture propagation model reported above (**Eq.9**). In this section we describe the experimental setup and procedure used for the hydraulic fracturing experiments. The testing apparatus is shown in **Figure 2**. The setup is composed of four key sub-systems:

a) Three independent and mutually orthogonal dual actuators to apply three independent and mutually orthogonal stresses on a cubic rock sample (**Fig.2b**).

b) Three hydraulic pumps to supply and independently regulate the hydraulic oil pressure in each dual actuator, and control the stress in that direction; and one additional pump to inject the fracturing fluid into the wellbore-sample assembly (**Fig.2a**).

c) Three Linear Variable Differential Transformers (LVDTs) attached to the dual actuators to measure the displacement along each stress direction.

d) A data acquisition system to monitor wellbore pressure with high-sensitivity pressure transducers (Keller X30) (**Fig.2c**).

In order to capture the strain energy dissipation with sufficient time resolution during the experiment, fracture propagation must be sufficiently slow.^{30,48} To achieve this, a Newtonian fluid with a relatively high viscosity (i.e., honey), and a low injection rate of 0.2 cc/min were used, while the borehole pressure evolution with time is monitored.³ Moreover, a micro-metric control needle valve V_i is used at the injection inlet to slow down the injected fluid, minimise turbulent flow into the wellbore/sample, and better mimic in the laboratory field injection conditions.^{30,49} The stress conditions prior to injection are maintained (regulated) at low confining case of $\sigma_V = 6.5$ MPa (940psi), $\sigma_H = 3$ MPa (440psi), $\sigma_h = 1.5$ MPa (220psi) or the higher case of $\sigma_V = 15$ MPa (2175psi), $\sigma_H = 10$ MPa (1450psi), $\sigma_h = 5$ MPa (725psi) at all times and for all the hydraulic fracturing experiments reported here.

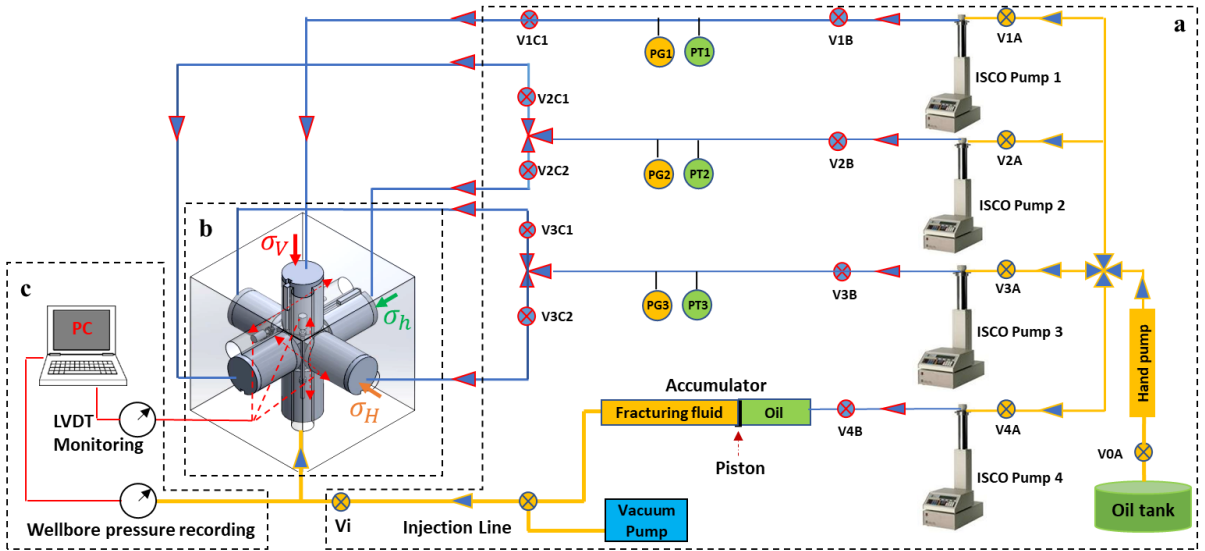


Fig.2 Schematic of hydraulic fracturing experimental setup: **a** Pumping system; **b** fracturing system; and **c** data acquisition system. *PT* pressure transducer, *PG* pressure gauge, *V* valve, *Vi* micro-meter valve, *LVDT* linear Variable Differential Transformer, *PC* computer.

4. Results

4.1 Hydro-mechanical data

The time of fracture initiation serves as a reference for the experimental evaluation of the energy partitioning during hydraulic fracturing. The borehole pressure BHP and the three mutually orthogonal strains derived from the measured displacements are normalized by their value at this specific time. The injection energy E_I (Eq.3) and the non-seismic deformation energy E_d (Eq.4) are calculated accordingly. **Figs.3 and 4** show a typical hydro-mechanical data set acquired during the hydraulic fracturing of a quartz-rich sample S_1 under the low ($\sigma_v = 6.5$ MPa, $\sigma_H = 3$ MPa, $\sigma_h = 1.5$ MPa), and high confinement ($\sigma_v = 15$ MPa, $\sigma_H = 10$ MPa, $\sigma_h = 5$ MPa), respectively; where by convention a negative (positive) strain indicates extension (compression). Overall, the time evolution of the three mutually orthogonal strains recorded during the experiment are significantly nonlinear. The horizontal tensile strain is essentially induced by the opening and propagation of the fracture (negative ε_h in green), whereas the vertical shortening is induced by the imposed vertical compressive stress σ_v simulating the overburden (positive ε_v in blue).

The evolution of the three strains as a function of the borehole pressure BHP for the samples under low confinement ($\sigma_v = 6.5$ MPa, $\sigma_H = 3$ MPa, and $\sigma_h = 1.5$ MPa) are shown in **Fig.5**. The magnitude of the strain ε_H along the maximum horizontal stress σ_H (orange curve) remains

relatively small compared to the other two strains (from sample S_1 to S_5); it also remains relatively constant throughout the experiment, although a small deflection can be observed when the magnitude of ε_h (green curve) and ε_V (blue curve) exhibit the significant change with BHP during fracture propagation. While for PMMA S_6 (**Fig.5f**), the strain ε_H shows a significant deflection comparing to that of other samples.

Under the higher confinement ($\sigma_V = 15$ MPa, $\sigma_H = 10$ MPa, and $\sigma_h = 5$ MPa) (**Fig.6**): The magnitude of the strain ε_H along the maximum horizontal stress σ_H (orange curve) shows slightly negative deflection for quartz-rich S_1 , mixed-average S_4 , and PMMA S_6 ; while the significantly positive compression are observed in clay-rich S_2 , the calcite-rich S_3 , and the clay-rich₂ S_5 . Interestingly, the largest magnitude of ε_h (green curve) and ε_V (blue curve) are observed for PMMA S_6 (**Fig.6f**), which is attributed to the shear-dilation failure with respect to the vertical stress (see **Fig.8f**).

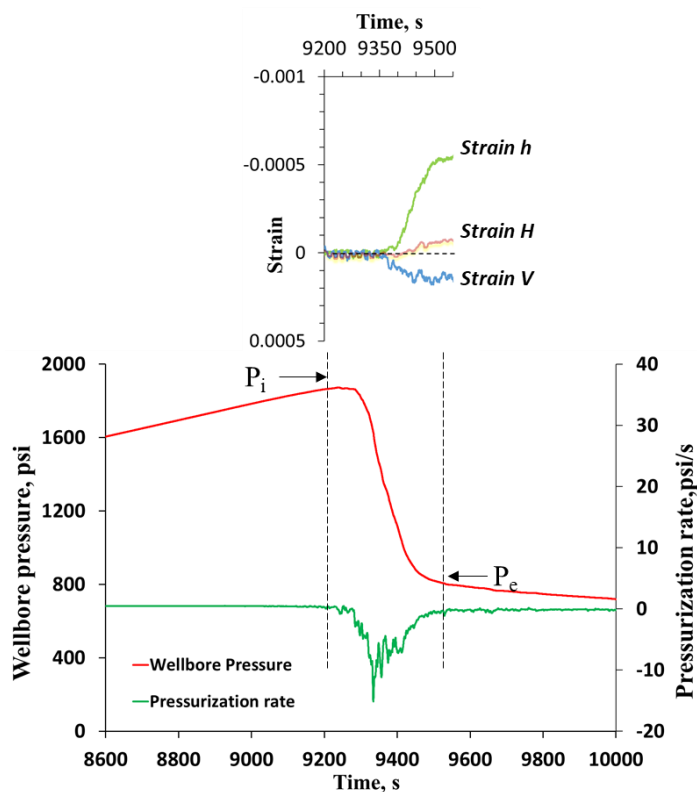


Fig.3. Synchronized wellbore pressure and strain data recorded during a representative hydraulic fracturing experiment (quartz-rich sample S_1) under $\sigma_V = 6.5$ MPa (940psi), $\sigma_H = 3$ MPa (440psi), and $\sigma_h = 1.5$ MPa (220psi). P_i and P_e denote the borehole pressure at the initiation and at the end of fracture propagation, respectively.

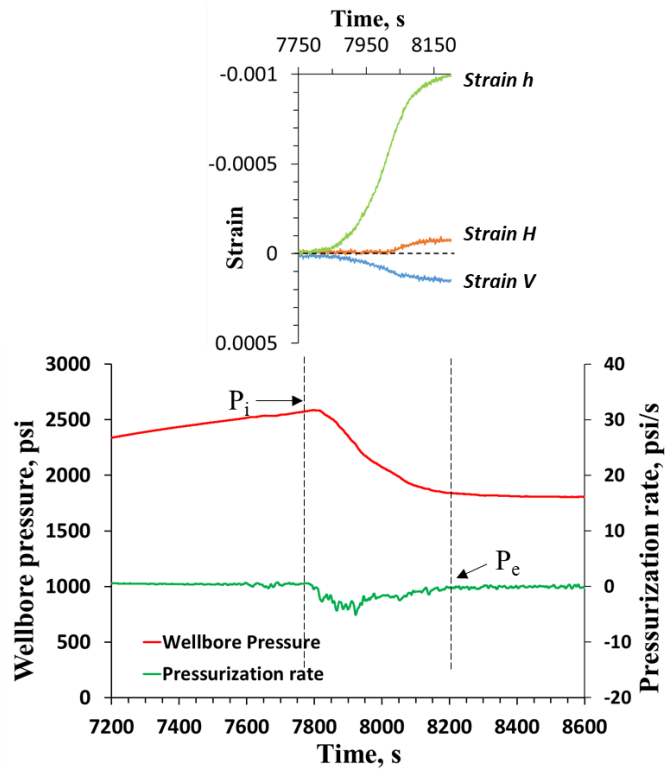


Fig.4 Synchronized wellbore pressure and strain data recorded during a representative hydraulic fracturing experiment (quartz-rich sample S_1) under $\sigma_v = 15$ MPa (2175psi), $\sigma_H = 10$ MPa (1450psi), and $\sigma_h = 5$ MPa (725psi). P_i and P_e denote the borehole pressure at the initiation and at the end of fracture propagation, respectively.

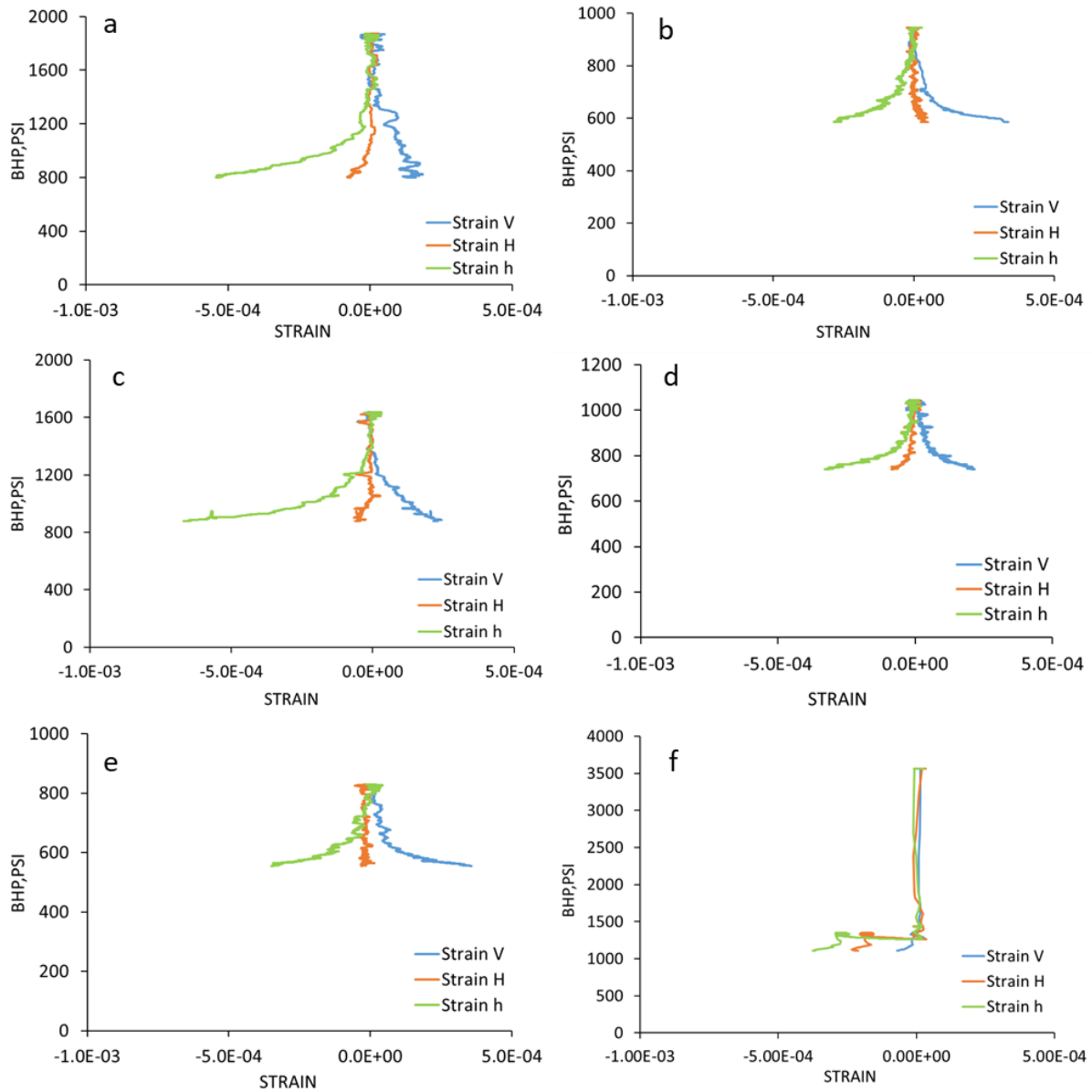


Fig.5. Fracture propagation scenario under low stress conditions of $\sigma_v = 6.5$ MPa, $\sigma_H = 3$ MPa, and $\sigma_h = 1.5$ MPa. Wellbore pressure and strain data recorded during hydraulic fracturing between fracture initiation at $BHP = P_i$, and the end of propagation at $BHP = P_e$ for: a) the quartz-rich sample S_1 , b) the clay-rich S_2 , c) the calcite-rich S_3 , d) mixed-average S_4 , e) the clay-rich₂ S_5 , and f) the PMMA S_6 .

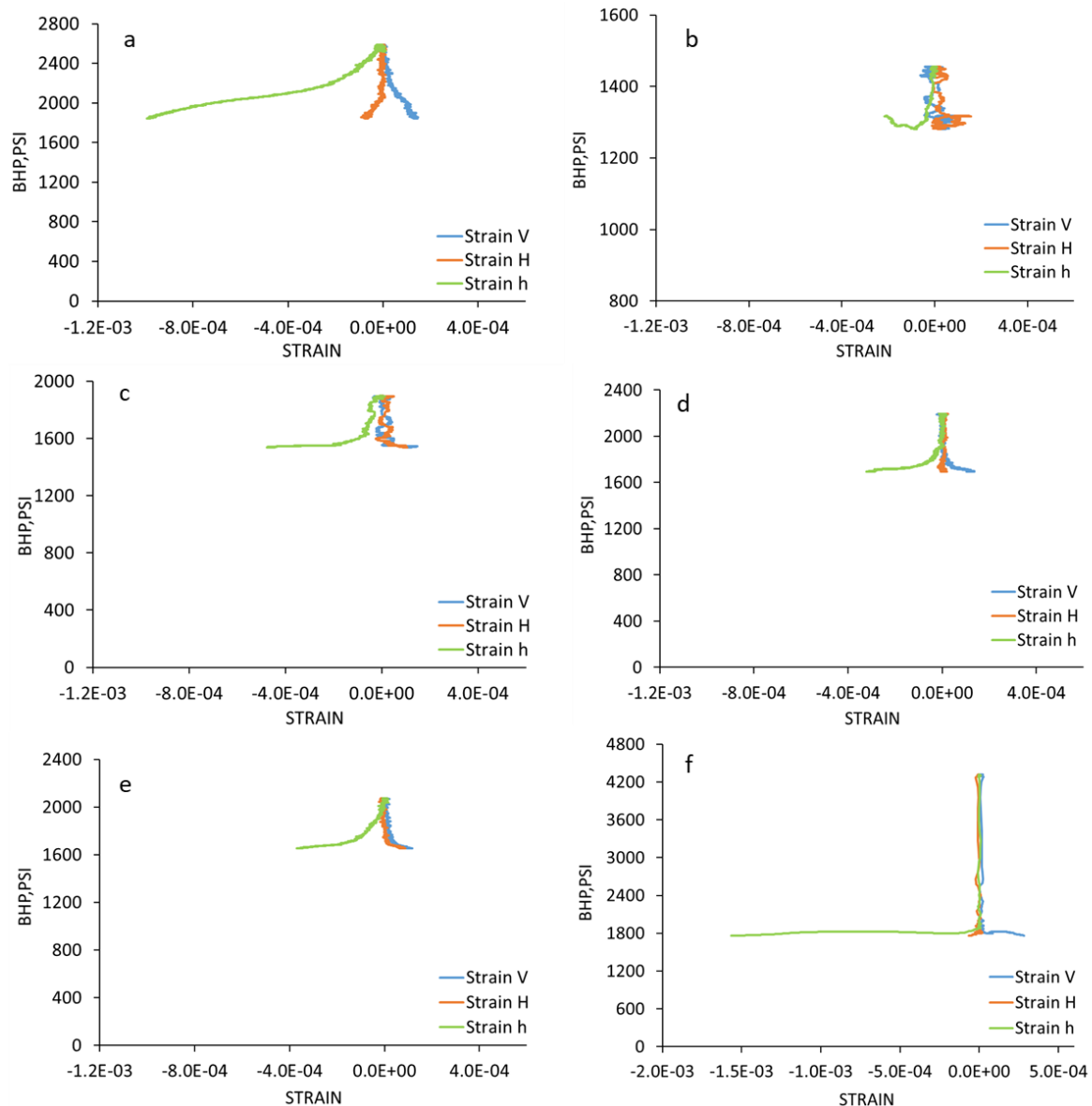


Fig.6. Fracture propagation scenario under high stress conditions of $\sigma_v = 15$ MPa, $\sigma_H = 10$ MPa, and $\sigma_h = 5$ MPa. Wellbore pressure and strain data recorded during hydraulic fracturing between fracture initiation at BHP = P_1 , and the end of propagation at BHP = P_e for: a) the quartz-rich sample S_1 , b) the clay-rich S_2 , c) calcite-rich S_3 , d) mixed-average S_4 , e) clay-rich₂ S_5 , and f) the PMMA S_6 .

4.2 Hydraulic fracture geometry

The representative photographs of the samples after hydraulic fracturing are shown in **Fig.7** (low confinement) and **Fig.8** (high confinement). It turns out that for clay-rich S_2 , the calcite-rich S_3 , and the clay-rich₂ S_5 the fracture is overall orthogonal to σ_h , as expected. However, for the quartz-rich S_1 (**Fig.7a** and **Fig.8a**), and the mixed-average S_4 (**Fig.7d** and **Fig.8d**) samples, the fracture is tilted with respect to both σ_H and σ_h . The most interesting observation is the vertically shear-opening fracture within PMMA S_6 under the high confinement (**Fig.8f**), rather than the horizontal opening mode observed for the lower confinement (**Fig.7f**). The repeatability of fracture geometry are reported in the **Appendix A**.

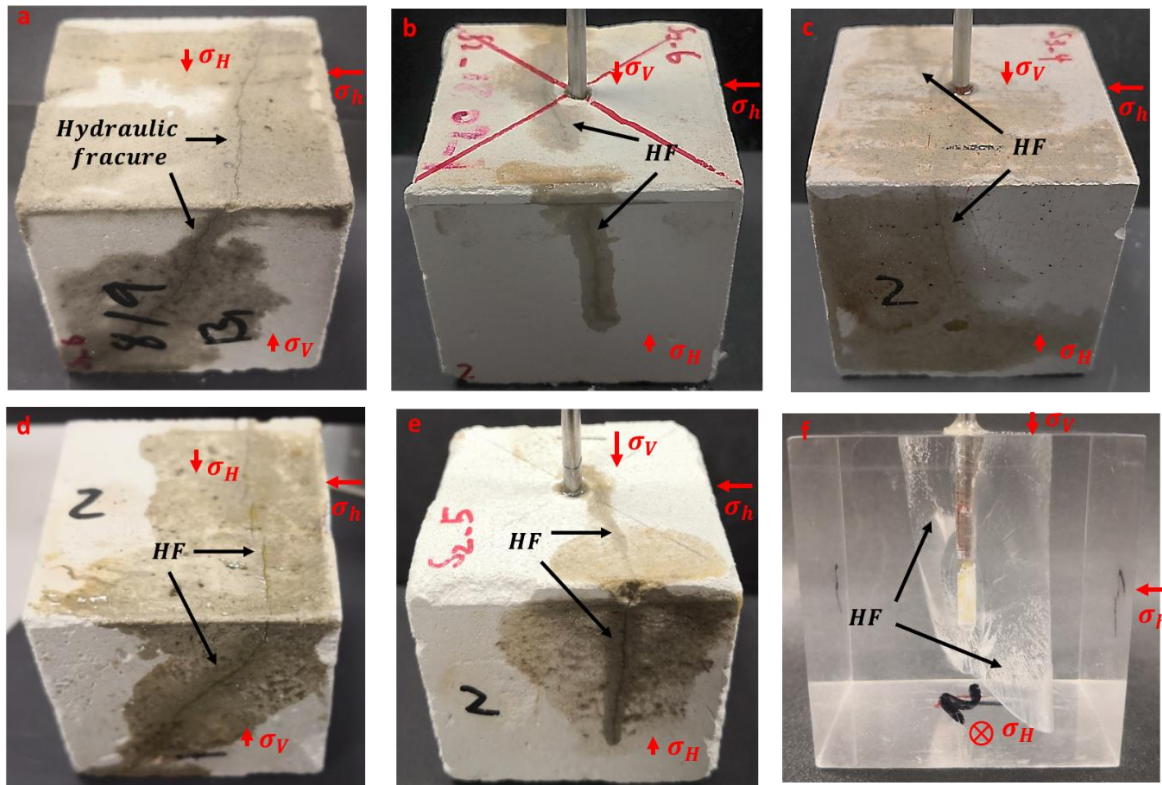


Fig.7. Fracture propagation scenario under low stress conditions of $\sigma_v = 6.5$ MPa, $\sigma_H = 3$ MPa, and $\sigma_h = 1.5$ MPa. Fractured samples from: a) the quartz-rich rock type S₁, b) the clay-rich S₂, c) the calcite-rich S₃, d) the mixed-average S₄, e) the clay-rich₂ S₅, and f) the PMMA sample.

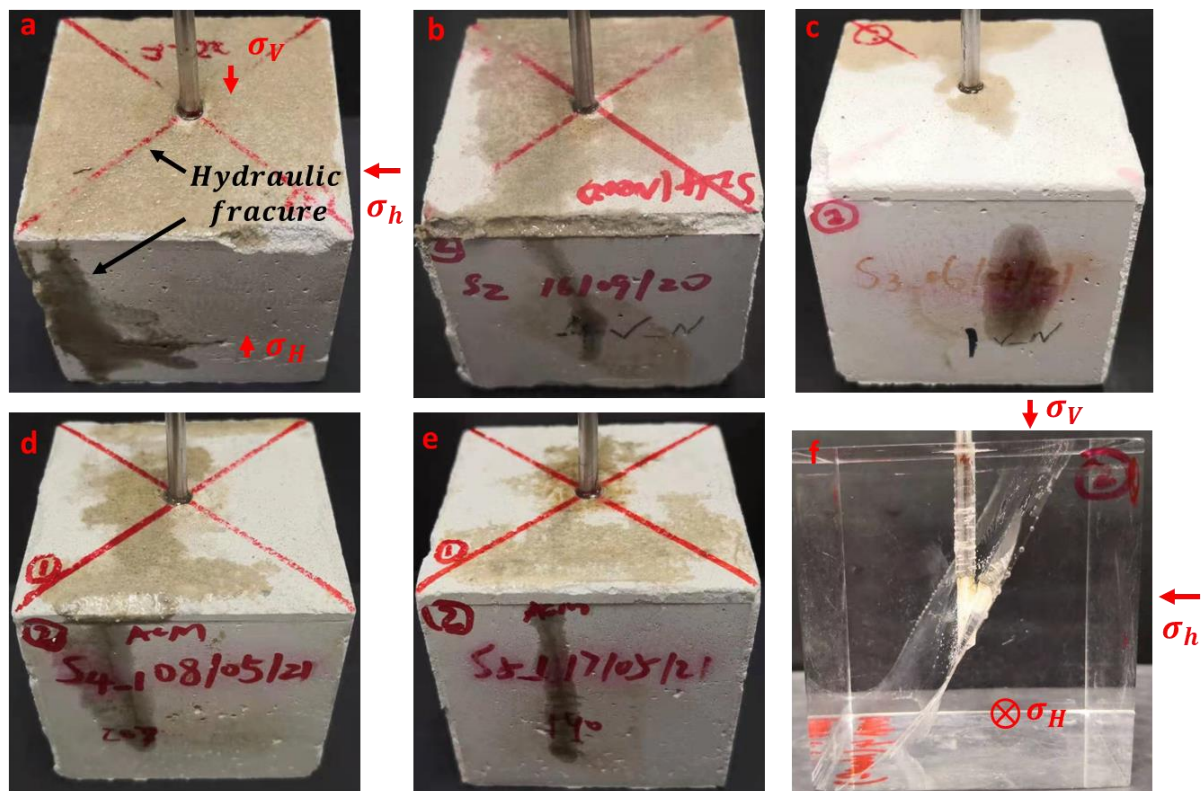


Fig.8. Fracture propagation scenario under high stress conditions of $\sigma_v = 15$ MPa, $\sigma_H = 10$ MPa, and $\sigma_h = 5$ MPa. Fractured samples from: a) the quartz-rich rock type S₁, b) the clay-rich S₂, c) the calcite-rich S₃, d) the mixed-average S₄, e) the clay-rich₂ S₅, and f) the PMMA sample.

4.3 Energy calculation and Brittleness Index

The injection energy E_I , non-seismic deformation energy E_d , and the energy partitioning ratio E_d/E_I are computed for the hydraulic fracturing experiments conducted on all mineral-cement mixtures and PMMA. The representative values for each material studied here are reported in **Table 1**. These results show that the clay-rich rock type S₂ exhibits the highest partitioning ratio ($E_d/E_I = 64.7\%$), followed by the clay-rich₂ S₅ (61.8%), the calcite-rich S₃ (55.8%), the mixed-average S₄ (43.4%), the quartz-rich S₁ (32.4%); and the lowest value was recorded for the PMMA S₆ (2.7%). We also observe that the partitioning ratio E_d/E_I for that of higher confinement ($\sigma_v = 15$ MPa, $\sigma_H = 10$ MPa, and $\sigma_h = 5$ MPa) is systematically higher than for a low confining case ($\sigma_v = 6.5$ MPa, $\sigma_H = 3$ MPa, and $\sigma_h = 1.5$ MPa). This ratio is the highest for the mineral-cement mixture S₂(90.6%), followed by S₅(86%), S₁(65.2%), and S₄(74%); it is significantly lower for S₃ (76.3%), and rather negligible for the PMMA S₆ (6.1%).

The brittleness indices BI_1 , BI_2 , and BI_3 were calculated using **Eqs.1, 2 and 5**, and are listed in **Table 2** for all six types of materials tested here. Note that the input parameters have been averaged prior to calculating BI_1 and BI_2 . In this study, the BI_1 is only assessed for zero confinement due to the technical limitations; while the BI_2 and BI_3 are quantified subjected to both low and higher confining cases.

These BI values are also compared in **Fig.9**. The trend of Rickman et al.'s BI_1 is partially agreed with BI_3 with respect to the samples of quartz-rich (S₁), calcite-rich (S₃) and mixed-average (S₄), however, it shows notable discrepancy among the samples of clay-rich (S₂ and S₅) as well as the most brittle material-PMMA (S₆). Overall, the BI_1 is higher than BI_2 and the new BI_3 for all sample types except the PMMA sample S₆; the most striking result is that the BI_1 model fails to quantitatively reflect the brittleness of PMMA sample (S₆). Under the low confinement, the Papanastasiou et al.'s BI_2 is systematically the lowest for all sample types. As the increase of total confinement (see **Fig.9**), the BI_2 shows an unexpected increase among the samples-clay-rich S₂, calcite-rich S₃, and clay-rich₂ S₅; but a nearly constant value for samples-quartz-rich S₁, and mix-average S₄; while a decreased value only for sample PMMA S₆.

The overall value of our BI_3 shows a reasonable decrease as the increase of confinement; and yield analogous trend across the tested materials studied (except for S₄) (**Fig.9**). Under the high confining case, BI_2 and BI_3 exhibited qualitative consistency of the trend among samples S₁₋₆. Their quantities are relatively consistent among S₁, S₄, and S₆; but a notable discrepancy exists among S₃, especially for the S₂ and S₅. For the higher confinement, the BI_3 yields the lowest

boundary of brittleness index (BI) for all synthetic samples (from S₁ to S₅). Interestingly, the BI based on BI_2 (under the low confinement) and BI_3 (under the high confinement) are shown to be quantitatively consistent, which is an unexpected result.

Table 1. Injection energy E_I , non-seismic deformation energy E_d , and energy partitioning ratio E_d/E_I calculated for the six materials studied here under both low and higher confinement (representative 5 mineral-cement mixtures and PMMA shown in Figs.7 and 8). Values outlined in bold represent the minimum and maximum for each reported parameter.

| Energy (J) | Quartz-rich (S ₁) | Clay-rich (S ₂) | Calcite-rich (S ₃) | Mixed Average (S ₄) | Clay-rich ₂ (S ₅) | PMMA (S ₆) |
|-------------------|----------------------------------|--------------------------------|-----------------------------------|------------------------------------|---------------------------------------------|---------------------------|
| E_I (Low Conf) | 123 | 51.3 | 101 | 58 | 42 | 279 |
| E_d (Low) | 40 | 33.2 | 56.4 | 25.2 | 25.8 | 7.4 |
| E_d/E_I (Low) | 32.4% | 64.7% | 55.8% | 43.4% | 61.8% | 2.7% |
| E_I (High Conf) | 182.5 | 80 | 104.6 | 130 | 117 | 413 |
| E_d (High) | 119 | 72.5 | 80 | 96 | 100.8 | 25.2 |
| E_d/E_I (High) | 65.2% | 90.6% | 76.3% | 74% | 86% | 6.1% |

Table 2. Brittleness index results for the six materials studied here under both low and higher confinement (5 mineral-cement mixtures and PMMA). For BI_1 and BI_2 , the requiring parameters have been normalized/averaged; Values outlined in bold represent the minimum and maximum for each reported parameter.

| BI model | Quartz-rich (S ₁) | Clay-rich (S ₂) | Calcite-rich (S ₃) | Mixed Average (S ₄) | Clay-rich ₂ (S ₅) | PMMA (S ₆) |
|----------------------|----------------------------------|--------------------------------|-----------------------------------|------------------------------------|---------------------------------------------|---------------------------|
| BI_1^* (Zero Conf) | 0.766 | 0.596 | 0.567 | 0.670 | 0.608 | 0.43 |
| BI_2 (Low Conf) | 0.373 | 0.107 | 0.242 | 0.294 | 0.182 | 0.945 |
| BI_3 (Low) | 0.68 | 0.35 | 0.44 | 0.566 | 0.38 | 0.974 |
| BI_2 (High Conf) | 0.342 | 0.23 | 0.324 | 0.33 | 0.3 | 0.82 |
| BI_3 (High) | 0.35 | 0.094 | 0.24 | 0.26 | 0.14 | 0.94 |

* BI_1 is investigated under zero confinement only

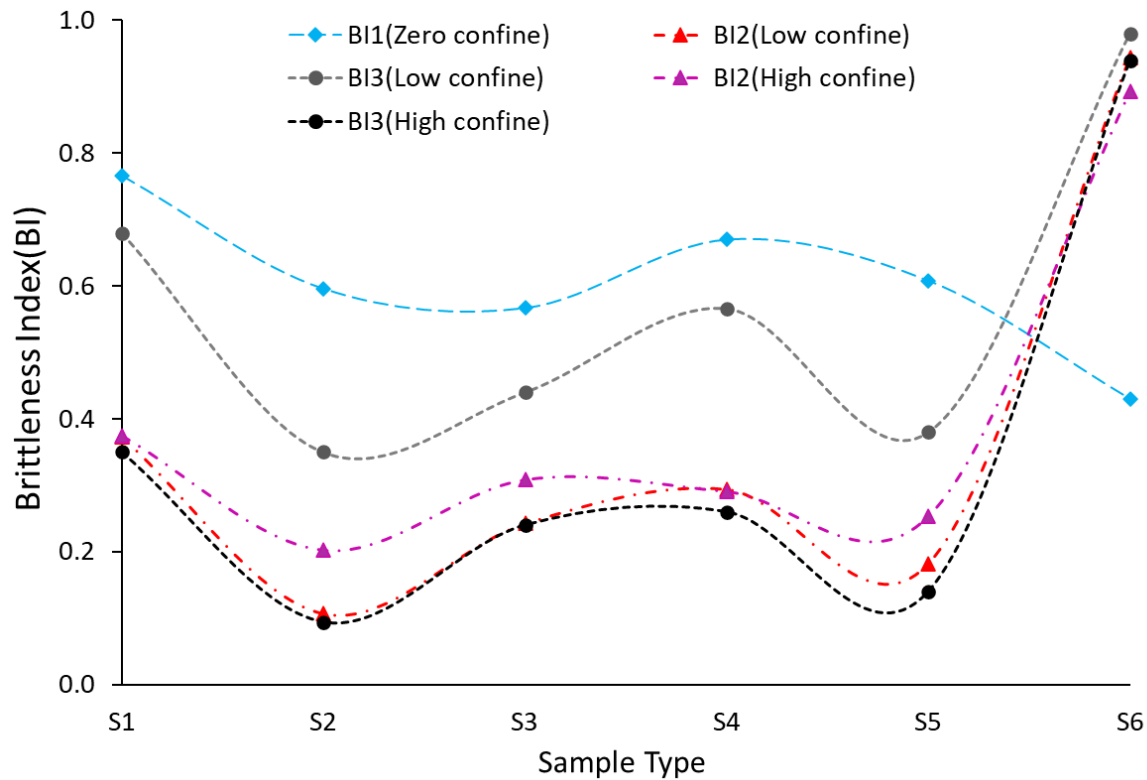


Fig.9. Brittleness index BI_1^* ; BI_2 and BI_3 versus investigated samples under the confinement of low ($\sigma_v = 6.5$ MPa, $\sigma_H = 3$ MPa, and $\sigma_h = 1.5$ MPa) and higher ($\sigma_v = 15$ MPa, $\sigma_H = 10$ MPa, and $\sigma_h = 5$ MPa). * BI_1 is investigated under zero confinement only

5. Discussion

5.1 Dependence of the brittleness index (BI) on fracture geometry

According to the BI quantification based on BI_2 and BI_3 (Table 2 or Fig.9), the six types of samples are classified as brittle PMMA S₆, semi-brittle quartz-rich S₁ and mixed-average S₄, semi-ductile calcite-rich S₃, and the ductile clay-rich S₂ and S₅. The geometry of hydraulic fracture (HF) indicate that for semi-ductile (S₃) and ductile samples (S₂ and S₅) the fracture propagation is nearly perpendicular to the minimum horizontal stress σ_h under either low (Figs.7b, c and e) or high confinement (Figs.8 b, c and e). However, for the semi-brittle samples (S₁ and S₄) the HF is always inclined to both σ_H and σ_h under either the low confinement (Figs.7a and d) or high confinement (Figs.8a and d). Interestingly, it is found that for semi-brittle samples S₁ and S₄ the HF geometry are still significantly inclined to both σ_H and σ_h (Figs.8a and d) even the quantified BI is shown to be significantly reduced under the high confinement (Fig.9). This is because the stronger stress effect (i.e., higher horizontal stress difference) on the samples plays a more significant role in the initiation and propagation

of the hydraulic fracture for semi-brittle samples under the higher confinement (i.e., $\sigma_h = 1.5$ MPa or $\sigma_v = 15$ MPa, $\sigma_H = 10$ MPa, $\sigma_h = 5$ MPa).

The most interesting observation is the hydraulic fracture inclined to both σ_v and σ_h for brittle PMMA (S_6) under the higher confine (**Fig.8f**), rather than that of inclination to both σ_H and σ_h under the low confinement (**Fig.7f**). This type of shear-dilation (i.e., mixed mode-I and II propagation scenario for **Fig.8f**) is also evidenced by the monitored strain data where the magnitude of vertical (ϵ_v) and horizontal strain (ϵ_h) (**Fig.6f**) are significantly higher than that of mode-I fracture (**Figs.5f** and **7f**). Such type of shear-dilation (**Fig.8f**) may be caused by the higher stress concentration at the fracture tip where the higher breakdown/propagation pressure (**Fig.6f**) is subjected to normal faulting regimes (i.e., $\sigma_v > \sigma_H > \sigma_h$).

The results also indicate that the propagation of a hydraulic fracture is associated with the intermediate stress, especially in brittle/semi-brittle samples (**Figs.5** and **6**). These observations reveal that the geometry of hydraulic fracture is highly dependent on the brittleness/ductility of the rock under true triaxial stress conditions. Such analogous phenomenon is also observed in a numerical study by Ju et al.⁵⁰

5.2 Applicability of the new and existing BI models

The comparison of the analysed *BI* models (**Fig.9**) suggests that BI_1 quantitatively overestimates the BI value (except for the striking lower BI value for PMMA), which is in good agreement with the previous study^{3,26}. Furthermore, Holt et al.²⁶ showed that the BI value from Rickman et al.²⁴ increases with confining pressure, which is contradicted to the physical observations where the rock brittleness (ductility) is expected to decrease (increase) with the increasing confinement.^{38,51} Therefore, the BI_1 could only provide qualitative analysis on limited rock types. However, the laboratory measurement/interpretation of both P-wave and S-wave velocity subjected to true-triaxial stresses is challenging.

Under the lower confinement (**Fig.9**), the BI_2 and BI_3 show a consistent trend among the different types of samples tested here; but the value of BI_2 is systematically lower than BI_3 . From the low to higher confinement, the unexpected increment of BI_2 is observed among the semi-ductile (S_3) and ductile samples (S_2 and S_5). Under the high confinement, the value of BI_2 shows a relatively quantitative agreement with the BI_3 among the brittle/semi-brittle samples (e.g., quartz-rich S_1 , mix-average S_4 , and PMMA S_6); a slight difference among the ductile/semi-ductile samples (e.g., clay-rich S_2 , calcite-rich S_3 , and clay-rich₂ S_5) (**Fig.9**). These observations indicates that the BI_2 offers a good qualitative analysis of the brittleness

among the samples exhibiting a wide range of rheology, and offers a good quantitative analysis for brittle/semi-brittle samples under the high confinement. Theoretically, the BI_2 model is only limited to mode-I fracture propagation²⁹. The applicability of BI_2 for mixed mode-I and mode-II hydraulic fracture is required to be further investigated.

These observations (**Fig.9**) reveal that our new proposed model BI_3 is stress-dependent and capable of capturing the brittle-to-ductile behaviour within a wide range of rheological samples subjected to hydraulic fracturing.

5.3 Estimation of the non-seismic deformation energy at laboratory and field scales

The model for the evolution of fracturing area A_d developed by our recent study (Feng et al⁴⁷) (i.e., **Eq.9**) allows for the robust estimation of the non-seismic deformation energy E_d associated with hydraulic fracture propagation (**Eq.4**). The ratio of the non-seismic deformation energy E_d to the total injection energy E_I ranges from 32 % to 91% (except for PMMA), which is slightly higher than (i) published field estimations (ranging from 15% to 80%, see Boroumand and Eaton;⁴⁰ Maxwell et al.;⁵² and Warpinski et al.⁵³); and comparable to (ii) laboratory-derived estimations in granite samples (ranging from 18% to 94%, see Goodfellow et al.⁴¹). The slight difference of E_d / E_I could be attributed to a) the presence of soft/weak minerals within the distinct samples used for the studies b) simplification of the temporal fracturing area A_d estimation in the previous studies.

5.4 Limitations and future developments

The prediction of the evolution of the temporal fracturing area (A_d) presented here assumes a 2D planar fracture geometry. The roughness of the fracture surface and the viscosity of the fluid are expected to impact fracture propagation³⁷. However, as shown in **Figs.A1d, A2d**, the simplified fracturing area A_d predicted is in good agreement with experimental measurements, demonstrating its applicability for different propagation scenarios at the laboratory scale (see details in Feng et al 2022).

The samples used in this study are homogeneous isotropic, which providing a benchmark for the more complicate samples where the heterogeneity or anisotropic exists (e.g., shale). The associated study are in progress and recommended for future study.

Honey was used as a viscous fracturing fluid in our experiments to ensures a laminar Newtonian flow into the fracture, and restrict the catastrophic fracture propagation at the lab scale^{3,30,49}. More sensitivity studies using low viscous fluid are recommended.

6. Conclusion

Quantification of the brittleness index (BI) is vital in a wide variety of underground engineering applications^{1,3-6,8,9,29,54-57}. Due to the uncertainties associated with existing *BI* models applied in the hydraulic fracturing associated applications, we developed a new brittleness index *BI*₃ based on hydro-mechanical energy criteria and backed by an exhaustive set of new laboratory data. In this study, we correlate the wellbore pressure and strain induced by hydraulic fracturing of the synthetic samples subjected to true triaxial stresses with either a low ($\sigma_v = 6.5$ MPa, $\sigma_H = 3$ MPa, and $\sigma_h = 1.5$ MPa), and a high (15 MPa, 10 MPa, and 5 MPa) confinement. An analytical model for the evolution of the fracturing area A_d ⁴⁷ is used to quantify the non-seismic deformation energy E_d associated with hydraulic fracture propagation, leading to a more robust quantification of the brittleness of the tested rocks subjected to hydraulic fracturing.

By comparing the BI quantified from our model (*BI*₃) to the existing models, i.e., a) based on sonic and density logs from Rickman et al.²⁴, and b) based on Mohr-Coulomb's brittle failure model from Papanastasiou et al.²⁹, we observed that the predictions based on our model (*BI*₃) are only qualitatively consistent with Papanastasiou et al.'s (*BI*₂), but less so with Rickman et al.'s (*BI*₁). Noteworthy, under the higher confinement, the value of *BI*₂ are relatively agreed with the *BI*₃ among the brittle/semi-brittle samples (e.g., quartz-rich S₁, mix-average S₄, and PMMA S₆); but a slight difference exists among the ductile/semi-ductile samples (e.g., clay-rich S₂, calcite-rich S₃, and clay-rich₂ S₅) (**Fig.9**). However, from the low to higher confinement, the *BI*₂ is unexpectedly increased among the semi-ductile (S₃) and ductile samples (S₂ and S₅). These comparison (**Fig.9**) reveals that our new proposed model *BI*₃ is stress-dependent and capable of capturing the brittle-to-ductile behaviour within a wide range of rheological samples subjected to hydraulic fracturing.

This study also reveals that the fracture geometry is highly dependent on not only the stress regimes, but also the brittleness/ductility of the rock, revealing the importance of BI evaluation prior to field applications. The quantification of energy terms associated with hydraulic fracturing (e.g., non-seismic deformation energy E_d , and Injection energy E_I) allow us to assess the brittleness index (BI) using the direct measurement (e.g., wellbore pressure, fracture width) from the laboratory or field test. Therefore, the new hydro-mechanical energy-based brittleness index model *BI*₃ are inherently advantageous in a wide range of underground applications involving hydraulic fracturing, e.g., economic production of unconventional energy resources.

Declaration of competing interest

The authors declare that they have no known competing interest

Acknowledgments

The first author sincerely thanks China Scholarship Council- Curtin International Postgraduate Research Scholarship (CSC-CIPRS, Grant No. 201808190001) for their financial support on this research.

Appendix A: Repeatability of the fracture geometry

Based on the brittleness index (BI) quantification listed in **Table 2** and **Fig.9**, it is found that for the brittle rock types- quartz-rich S_1 (**Figs.7a** and **8a**), and mixed-average S_4 (**Figs.7d** and **8d**), the tested samples exhibited a fracture plane tilted with respect to both σ_H and σ_h ; while for the less brittle rock types (e.g., clay-rich S_2 , and calcite-rich S_3), the orientation of fracture is nearly perpendicular to the σ_h . To assess the repeatability of our hydraulic fracturing experiments under true triaxial stresses, and better understand the conditions for which orthogonal or tilted fracture propagation occurs in these rock types, we conducted repeat experiments with additional samples under the same testing conditions.

The resulting fractured samples are shown in **Figs.A1** and **A2**. It can be seen that the fracture orientation for the quartz-rich S_1 (**Figs. A1a** and **A2a**) and the mixed-average S_4 (**Figs. A1d** and **A2d**) samples are repeatable, i.e., significantly tilted with respect to both σ_H and σ_h . In contrast, the calcite-rich sample S_3 (**Figs. A1c** and **A2c**) exhibits a significantly less tilted fracture; and the clay-rich sample S_2 (**Figs. A1b** and **A2b**) shows a nearly orthogonal fracture orientation.

It turns out that the results of the additional tests suggest a good repeatability in terms of fracture orientation. Note that in this manuscript the estimations of the new Brittleness Index BI_3 (**Table 2**) are based on the combination of all test data, including the repeat tests.

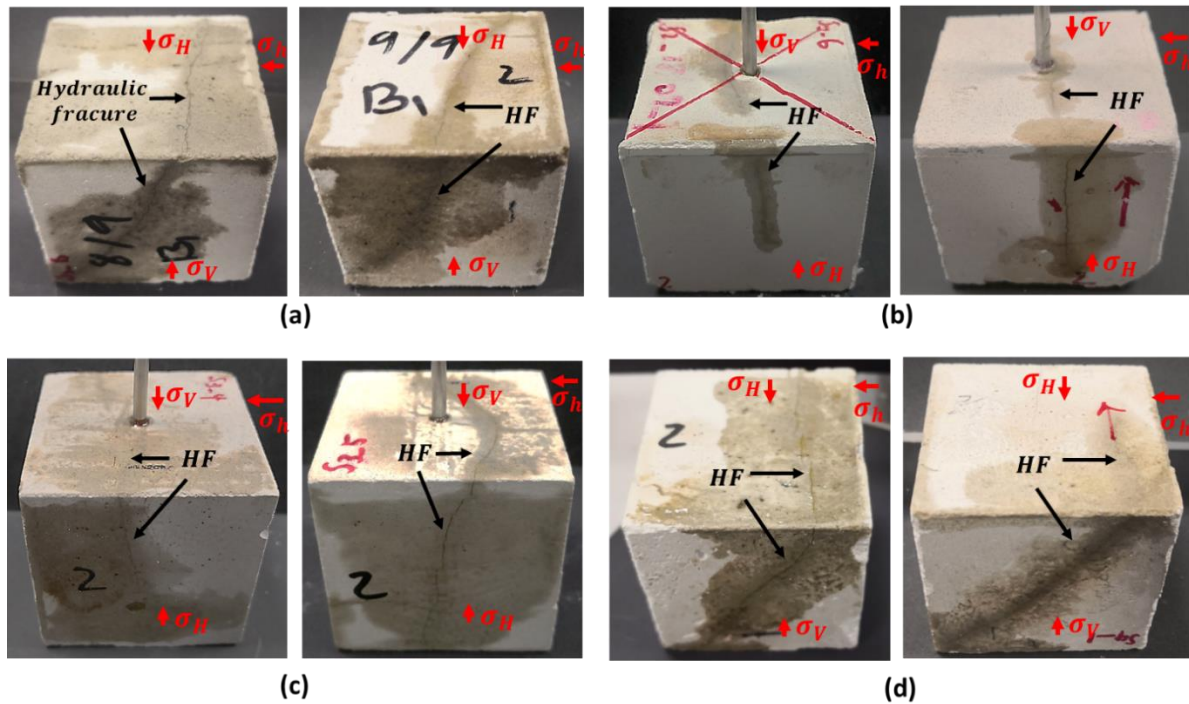


Fig.A1. Fracture orientation for the repeat tests under low $\sigma_v = 6.5$ MPa, $\sigma_H = 3$ MPa, and $\sigma_h = 1.5$ MPa: (a) quartz-rich (S_1), (b) clay-rich(S_2), (c) calcite-rich (S_3), (d) mixed-average(S_4).

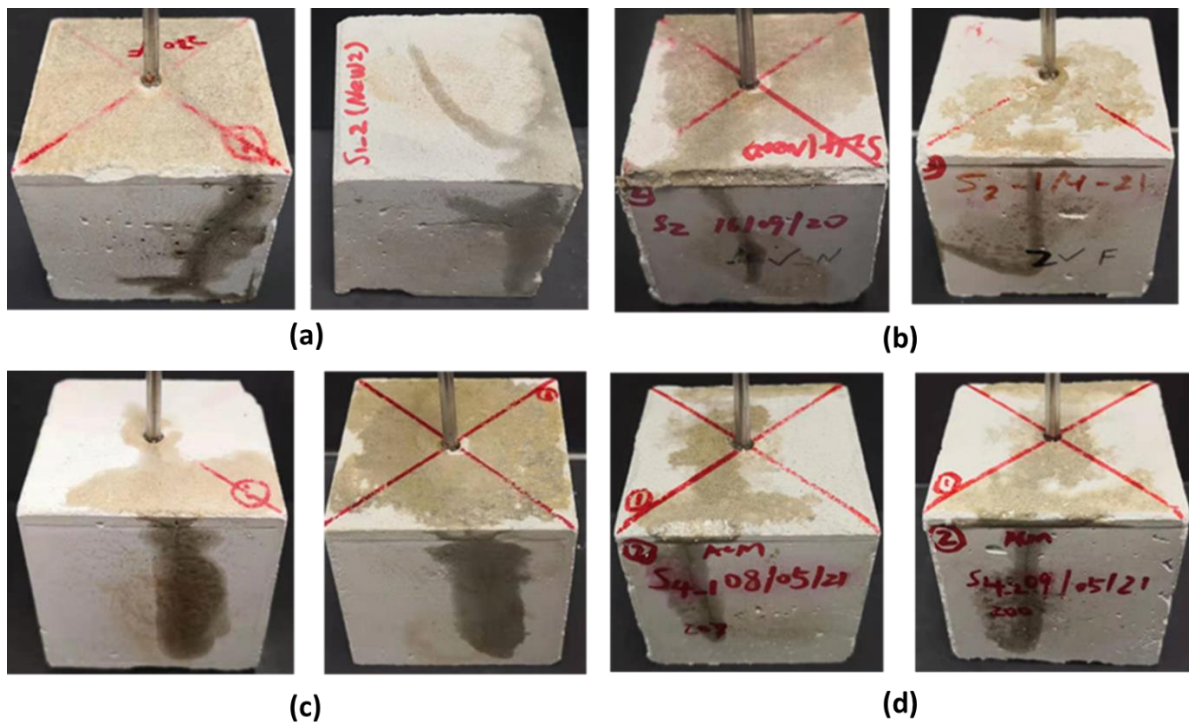


Fig.A2. Fracture orientation for the repeat tests under high $\sigma_v = 15$ MPa, $\sigma_H = 10$ MPa, and $\sigma_h = 5$ MPa: (a) quartz-rich (S_1), (b) clay-rich(S_2), (c) calcite-rich (S_3), (d) mixed-average(S_4).

Appendix B: Test Materials and Mechanical properties

B.1 Test materials & mechanical tests

To minimise the impact of heterogeneity, bedding, and defects usually found in natural rocks, we used in this study synthetic rock blocks made of silica, clay, and calcite mineral mixtures, with variable relative fractions. These minerals are most commonly found in geological materials in the Earth's crust such as shales, sandstones, and limestones⁵⁸⁻⁶¹. Standard Portland cement was added to the mineral mixtures as a bonding agent for its small grain size and low toughness.⁶² Blocks were moulded, out of which multiple plugs and cubic samples were extracted after cement curing. The details of the mineral composition and density of the various mixtures are listed in **Table B1**. More details on the samples fabrication procedures can be found in Feng et al.³; and Sarmadivaleh and Rasouli⁴⁹. In addition to the mineral-cement mixtures listed in **Table B1**, a block of PMMA was used as an ideally homogeneous and brittle rock analogue.⁶³⁻⁶⁵

The complete sample set, including mineral-cement mixtures and PMMA, comprises a) 25 cylindrical sample plugs 36 mm in diameter and 72 mm in height, used for estimating the mechanical properties of each material, i.e., 10 unconfined (UCS) and 25 triaxial (TCS) compression tests on dry samples; and b) 25 initially dry cubic samples 50x50x50 mm³ in size, used for hydraulic fracturing tests under true triaxial stress conditions. The TCS tests were conducted in dry conditions at 0.6, 2.1, and 3.4 MPa confining pressure. More details of mechanical testing procedure can be found in Feng et al.³ and Sarmadivaleh and Rasouli.⁴⁹ At least five samples of each mineral-cement mixture were prepared for testing (part of the samples is shown in **Fig.B1a**). The schematic of a cubic sample assembly during a typical hydraulic fracturing test is shown in **Fig.B1b**, along with the fluid injection wellbore and casing. A vertical 33 mm long wellbore is drilled into the sample, and the casing is introduced and glued to the wellbore down to one-third of the sample's height (17 mm below the sample's top surface), leaving an open hole section of 16 mm. Due to the extremely high tensile strength (above 60MPa) of PMMA⁶⁶, the wellbore in the impermeable PMMA cubes is notched at half the height of the sample to assist fracture initiation (25 mm below the sample's top surface).

Table B1. Composition and density of the five synthetic rock formulations (mineral cement mixtures) used in this study.

| Mineral-cement mixture | Silica (%) | Kaolinite (%) | Calcite (%) | Cement (%) | Density(g/cm ³) |
|-------------------------------|------------|---------------|-------------|------------|-----------------------------|
| Quartz-rich(S ₁) | 52.5% | 22.5% | 0.0% | 25% | 1.58 |
| Clay-rich(S ₂) | 22.5% | 52.5% | 0.0% | 25% | 1.26 |
| Calcite-rich(S ₃) | 15.0% | 7.5% | 52.5% | 25% | 1.44 |

| | | | | | |
|------------------------------------------|-------|-------|-------|-----|------|
| Mixed average(S ₄) | 30.0% | 22.5% | 22.5% | 25% | 1.50 |
| Clay-rich ₂ (S ₅) | 30.0% | 45% | 0.0% | 25% | 1.46 |

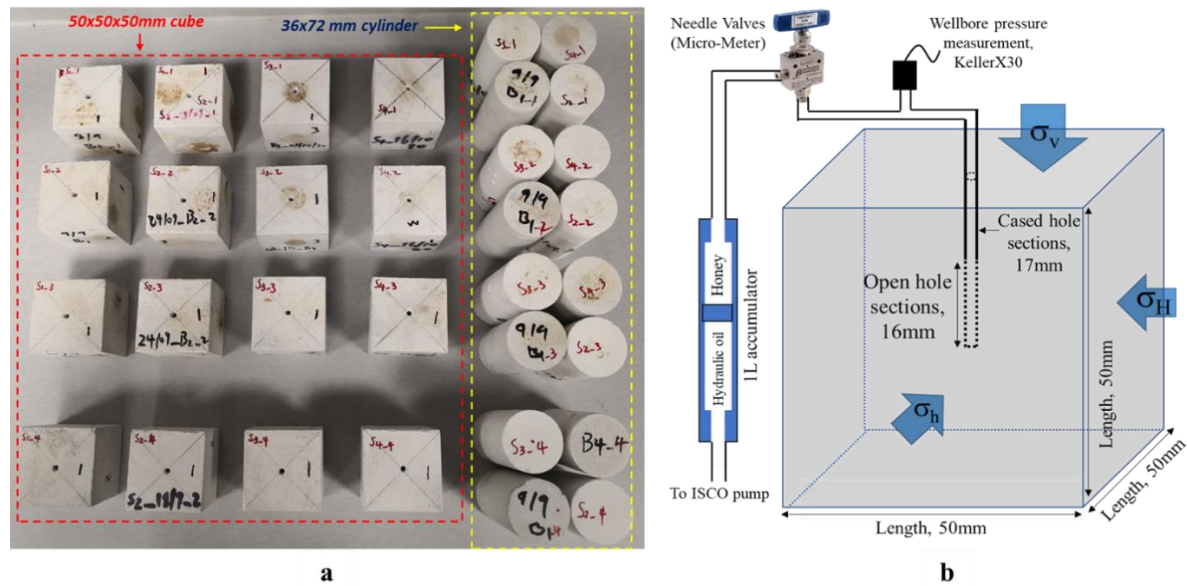


Fig.B1 Part of the synthetic rock samples used in this study: a) 50x50x50mm cubes for hydraulic fracturing, and 36x72mm cylindrical plugs for mechanical characterisation; b) schematic of a typical cubic sample prepared for hydraulic fracturing tests (modified from Feng et al. (2020)).

B.2 Mechanical and petrophysical properties

The mechanical properties of the mineral-cement mixtures used in this study (see **Table B1**) are shown in **Table B2**. Details of the procedures for UCS and TCS testing used to determine these values can be found in Feng et al.³ Young's modulus E ranges between 1.5 and 6.9 GPa, where the quartz-rich mixture S_1 exhibits the highest value, followed by the PMMA S_6 , the calcite-rich mixture S_3 , the mixed-average mixture S_4 , the clay-rich mixture S_2 , and the lowest value was found for the clay-rich₂ mixture S_5 . Poisson's ratio ranges from 0.39 for PMMA, down to 0.1 for the clay-rich mixture S_2 ; while mixtures S_1 , S_5 , S_4 , and S_3 exhibit intermediate values comprised between 0.17 and 0.21. The internal friction angle Φ ranges between 14.4° for PMMA and 42° for the quartz-rich mixture S_1 ; and the cohesion C_o is comprised between 0.6 MPa for the clay-rich mixture S_2 and 44.6MPa for PMMA. Ultrasonic compressional and shear wave velocities (V_P and V_S , respectively) at room conditions are higher in the stiffer mixtures S_1 and S_6 than in the clay-rich mixtures S_2 and S_5 . To the first order, this is attributed to the attenuation of acoustic wave by clay minerals.^{67,68}

Table B2. Mechanical properties of the mineral-cement mixtures and PMMA used in this study, and determined through unconfined (UCS) and triaxial (TCS) compression tests.

| Mineral-cement mixture | Young's modulus E (GPa) | Poisson's ratio ν (-) | Friction angle Φ ($^\circ$) | Cohesion C_o (MPa) | P-wave velocity | S-wave velocity | Porosity ϕ (-) |
|------------------------|---------------------------|---------------------------|------------------------------------|----------------------|-----------------|-----------------|---------------------|
|------------------------|---------------------------|---------------------------|------------------------------------|----------------------|-----------------|-----------------|---------------------|

| | | | | | V_P (km/s) | V_S (km/s) | |
|--------------------------------|-------|--------|--------|--------|-----------------|-----------------|------|
| Quartz-rich(S ₁) | 6.9* | 0.17* | 42* | 1.76* | 2.1 | 1.4 | 0.29 |
| Clay-rich(S ₂) | 2.6* | 0.1* | 35.3* | 0.6* | 1.3 | 0.87 | 0.3 |
| Calcite-rich(S ₃) | 3.2* | 0.21* | 40.9* | 0.9* | 1.69 | 1.07 | 0.2 |
| Mixed average(S ₄) | 3.0* | 0.18* | 35.8* | 1.5* | 1.8 | 1.17 | 0.24 |
| Clay-rich2(S ₅) | 1.6* | 0.17* | 37.3* | 0.8* | 1.47 | 0.97 | 0.3 |
| PMMA(S ₆) | 6.2** | 0.39** | 14.4** | 44.6** | 2.75 | 1.4 | 0 |

* UCS tests are conducted on dry samples, and TCS tests are conducted in dry conditions at 0.6, 2.1, and 3.4 MPa confining pressure.

** Data reported in the literature.

Abbreviations

| | |
|-----------|------------------------------------------|
| BI | Brittleness index |
| BI_n | Brittleness index model |
| HF | Hydraulic fracturing |
| TTSC | True tri-axial stress condition |
| TTSCs | True tri-axial stress cell |
| LVDT | linear Variable Differential Transformer |
| UCS | Uniaxial compressive strength |
| TCS | Triaxial compressive strength |
| BHP | Bottom-hole pressure |
| S_{1-6} | Type of sample |
| PMMA | Polymethyl Methacrylate |
| md | MiliDracy |

Nomenclature

| | |
|--------------|------------------------------------------------------------------------|
| E | Young's modulus |
| ν | Poisson's ratio |
| E_{dyn} | Dynamic Young's modulus |
| ν_{dyn} | Dynamic Poisson's ratio |
| Φ | Internal friction angle |
| C_o | Cohesion |
| σ_T | Tensile strength |
| σ_v | Vertical stress |
| σ_H | Maximum horizontal stress |
| σ_h | Minimum horizontal stress |
| σ_r | Resultant principle stress |
| ϵ_h | Hydraulic fracture induced strain with respect to σ_h direction |
| ϵ_H | Hydraulic fracture induced strain with respect to σ_H direction |
| L_h | Sample length with respect to σ_h direction |
| L_H | Sample length with respect to σ_H direction |
| θ | Inclination angle |
| w | Resultant width induced by hydraulic fracture |
| Q | Constant injection rate supplied by pump |
| q | Flow rate per unit perimeter |
| P_f | Fluid pressure |
| u | Fluid velocity |
| P | Wellbore pressure |

| | |
|------------------|-----------------------------------------------------------------------------------------|
| w | Width of hydraulic fracture |
| μ_f | Viscosity of fracturing fluid |
| $(\Delta A_R)_m$ | Incremental increase in fracture surface area per unit time increment Δt_m |
| A_T | Total fractured area |
| A_d | Temporally fracturing area |
| ϕ | Porosity |
| μ | Viscosity |
| E_I | Injection Energy |
| E_d | Non-seismic deformation energy according to fracture propagation |
| E_k | Kinetic energy |
| E_r | Radiated energy |
| P_b | Breakdown pressure |
| P_e | BHP pressure when hydraulic fracture reaches the boundary |
| $P(t)$ | Wellbore pressure during injection time period |
| $P(w)$ | Wellbore pressure corresponding to width from fracture initiation to end of propagation |
| t_b | Time of breakdown |
| t_f | Time at end of hydraulic fracture propagation |

Reference

1. Bakhshi E, Golsanami N, Chen L. Numerical Modeling and Lattice Method for Characterizing Hydraulic Fracture Propagation: A Review of the Numerical, Experimental, and Field Studies. *Archives of Computational Methods in Engineering*. 2020;1-32.
2. Barenblatt GI. The mathematical theory of equilibrium cracks in brittle fracture. *Advances in applied mechanics*. Elsevier; 1962:55-129.
3. Feng R, Zhang Y, Rezagholilou A, Roshan H, Sarmadivaleh M. Brittleness Index: from conventional to hydraulic fracturing energy model. *Rock Mechanics and Rock Engineering*. 2020;53(2):739-753.
4. Huang C, Chen S. Effects of Ductility of Organic-Rich Shale on Hydraulic Fracturing: A Fully Coupled Extended-Finite-Element-Method Analysis Using a Modified Cohesive Zone Model. *SPE Journal*. 2020;
5. Iyare U, Blake O, Ramsook R. Brittleness evaluation of Naparima Hill mudstones. *Journal of Petroleum Science and Engineering*. 2021;196:107737.
6. Amitrano D. Brittle-ductile transition and associated seismicity: Experimental and numerical studies and relationship with the b value. *Journal of Geophysical Research: Solid Earth*. 2003;108(B1)
7. Qu H, Wu X, Huang P, Tang S, Wang R, Hu Y. Acoustic Emission and Failure Characteristics of Shales with Different Brittleness Under AWJ Impingement. *Rock Mechanics and Rock Engineering*. 2022;55(4):1871-1886.
8. Shapiro SA. *Fluid-induced seismicity*. Cambridge University Press; 2015.
9. Weinberg RF, Regenauer-Lieb K. Ductile fractures and magma migration from source. *Geology*. 2010;38(4):363-366.
10. Altindag R, Guney A. Predicting the relationships between brittleness and mechanical properties (UCS, TS and SH) of rocks. *Scientific research and Essays*. 2010;5(16):2107-2118.
11. Hucka V, Das B. Brittleness determination of rocks by different methods. Elsevier; 1974:389-392.
12. Tarasov B, Potvin Y. Universal criteria for rock brittleness estimation under triaxial compression. *International Journal of Rock Mechanics and Mining Sciences*. 2013;59:57-69.

13. Hajiabdolmajid V, Kaiser P. Brittleness of rock and stability assessment in hard rock tunneling. *Tunnelling and Underground Space Technology*. 2003;18(1):35-48.
14. Steiner W, Kaiser PK, Spaun G. Role of brittle fracture in swelling behaviour: evidence from tunnelling case histories/Sprödbbruch in wenig festem Fels als Auslöser von Quellvorgängen: Erkenntnisse aus Fallstudien. *Geomechanics and Tunneling*. 2011;4(2):141-156.
15. Yagiz S, Yazitova A, Karahan H. Application of differential evolution algorithm and comparing its performance with literature to predict rock brittleness for excavatability. *International Journal of Mining, Reclamation and Environment*. 2020;34(9):672-685.
16. Dautriat J, Gland N, Dimanov A, Raphanel J. Hydromechanical behavior of heterogeneous carbonate rock under proportional triaxial loadings. *Journal of Geophysical Research: Solid Earth*. 2011;116(B1)
17. He W, Chen Z, Shi H, Liu C, Li S. Prediction of acoustic wave velocities by incorporating effects of water saturation and effective pressure. *Engineering Geology*. 2021;280:105890.
18. Li Y, Zhou L, Li D, et al. Shale Brittleness Index Based on the Energy Evolution Theory and Evaluation with Logging Data: A Case Study of the Guandong Block. *ACS omega*. 2020;5(22):13164-13175.
19. Liu Y, Yin G, Li M, et al. Mechanical properties and failure behavior of dry and water-saturated anisotropic coal under true-triaxial loading conditions. *Rock Mechanics and Rock Engineering*. 2019:1-20.
20. Minaeian V, Dewhurst DN, Rasouli V. Deformational behaviour of a clay-rich shale with variable water saturation under true triaxial stress conditions. *Geomechanics for Energy and the Environment*. 2017;11:1-13.
21. Sarout J, Esteban L, Delle Piane C, Maney B, Dewhurst DN. Elastic anisotropy of Opalinus Clay under variable saturation and triaxial stress. *Geophysical Journal International*. 2014;198(3):1662-1682.
22. Sarout J, Guéguen Y. Anisotropy of elastic wave velocities in deformed shales: Part 1—Experimental results. *Geophysics*. 2008;73(5):D75-D89.
23. Sarout J, Guéguen Y. Anisotropy of elastic wave velocities in deformed shales: Part 2—Modeling results. *Geophysics*. 2008;73(5):D91-D103.
24. Rickman R, Mullen MJ, Petre JE, Grieser WV, Kundert D. A practical use of shale petrophysics for stimulation design optimization: All shale plays are not clones of the Barnett Shale. Society of Petroleum Engineers; 2008:
25. Cho* D, Perez M. Rock quality assessment for hydraulic fracturing: A rock physics perspective. *SEG Technical Program Expanded Abstracts 2014*. Society of Exploration Geophysicists; 2014:2814-2818.
26. Holt RM, Fjær E, Stenebråten JF, Nes O-M. Brittleness of shales: relevance to borehole collapse and hydraulic fracturing. *Journal of Petroleum Science and Engineering*. 2015;131:200-209.
27. Perez Altamar R, Marfurt K. Mineralogy-based brittleness prediction from surface seismic data: Application to the Barnett Shale. *Interpretation*. 2014;2(4):T255-T271.
28. Zhang D, Ranjith P, Perera M. The brittleness indices used in rock mechanics and their application in shale hydraulic fracturing: A review. *Journal of Petroleum Science and Engineering*. 2016;143:158-170.
29. Papanastasiou P, Papamichos E, Atkinson C. On the risk of hydraulic fracturing in CO₂ geological storage. *International Journal for Numerical and Analytical Methods in Geomechanics*. 2016;40(10):1472-1484.
30. Bungler AP. *Near-surface hydraulic fracture*. University of Minnesota; 2005.

31. Liu S, Thoeni K, Feng R, Bona A, Sarmadivaleh M. Microstructure-based Modelling of Hydraulic Fracturing in silicified metamorphic rock using the Cohesive Element Method. *Engineering Fracture Mechanics*. 2022:108912.
32. Papanastasiou P. The influence of plasticity in hydraulic fracturing. *International Journal of Fracture*. 1997;84(1):61-79.
33. Salimzadeh S, Khalili N. A three-phase XFEM model for hydraulic fracturing with cohesive crack propagation. *Computers and Geotechnics*. 2015;69:82-92.
34. Yan C, Jiao Y-Y, Zheng H. A fully coupled three-dimensional hydro-mechanical finite discrete element approach with real porous seepage for simulating 3D hydraulic fracturing. *Computers and Geotechnics*. 2018;96:73-89.
35. Yan C, Zheng H. Three-dimensional hydromechanical model of hydraulic fracturing with arbitrarily discrete fracture networks using finite-discrete element method. *International Journal of Geomechanics*. 2017;17(6):04016133.
36. Karato S-i. Deformation of earth materials. *An Introduction to the Rheology of Solid Earth*. 2008;463
37. Liu D, Lecampion B. Propagation of a plane-strain hydraulic fracture accounting for a rough cohesive zone. *Journal of the Mechanics and Physics of Solids*. 2021;149:104322.
38. Wong T-f, Baud P. The brittle-ductile transition in porous rock: A review. *Journal of Structural Geology*. 2012;44:25-53.
39. Yang S-Q, Jing H-W, Wang S-Y. Experimental investigation on the strength, deformability, failure behavior and acoustic emission locations of red sandstone under triaxial compression. *Rock mechanics and rock engineering*. 2012;45(4):583-606.
40. Boroumand N, Eaton DW. Comparing energy calculations-hydraulic fracturing and microseismic monitoring. European Association of Geoscientists & Engineers; 2012:cp-293-00090.
41. Goodfellow S, Nasser M, Maxwell S, Young R. Hydraulic fracture energy budget: Insights from the laboratory. *Geophysical Research Letters*. 2015;42(9):3179-3187.
42. Van Der Baan M, Eaton D, Dusseault M. Microseismic monitoring developments in hydraulic fracture stimulation. International Society for Rock Mechanics and Rock Engineering; 2013:
43. Batchelor CK, Batchelor G. *An introduction to fluid dynamics*. Cambridge university press; 2000.
44. Lecampion B, Desroches J, Jeffrey RG, Bungler AP. Experiments versus theory for the initiation and propagation of radial hydraulic fractures in low-permeability materials. *Journal of Geophysical Research: Solid Earth*. 2017;122(2):1239-1263.
45. Bungler AP, Gordeliy E, Detournay E. Comparison between laboratory experiments and coupled simulations of saucer-shaped hydraulic fractures in homogeneous brittle-elastic solids. *Journal of the Mechanics and Physics of Solids*. 2013;61(7):1636-1654.
46. Garagash DI. Cohesive-zone effects in hydraulic fracture propagation. *Journal of the Mechanics and Physics of Solids*. 2019;133:103727.
47. Feng R, Sarout J, Dautriat J, Zhang J, Roshan H, Rezaee R, Sarmadivaleh M (2022). Data-constrained analytical model for the propagation of a penny-shaped hydraulic fracture under true triaxial stresses. doi.org/10.21203/rs.3.rs-1525036/v3
48. Sun C, Jin Z-H. Modeling of composite fracture using cohesive zone and bridging models. *Composites science and technology*. 2006;66(10):1297-1302.
49. Sarmadivaleh M, Rasouli V. Test design and sample preparation procedure for experimental investigation of hydraulic fracturing interaction modes. *Rock Mechanics and Rock Engineering*. 2015;48(1):93-105.

50. Ju Y, Wu G, Wang Y, Liu P, Yang Y. 3D Numerical Model for Hydraulic Fracture Propagation in Tight Ductile Reservoirs, Considering Multiple Influencing Factors via the Entropy Weight Method. *SPE Journal*. 2021;1-18.
51. Evans B, Fredrich JT, Wong TF. The brittle-ductile transition in rocks: Recent experimental and theoretical progress. *The brittle-ductile transition in rocks*. 1990;56:1-20.
52. Maxwell SC, Shemeta JE, Campbell E, Quirk DJ. Microseismic deformation rate monitoring. OnePetro; 2008:
53. Warpinski NR, Du J, Zimmer U. Measurements of hydraulic-fracture-induced seismicity in gas shales. Society of Petroleum Engineers; 2012:
54. Legarth B, Huenges E, Zimmermann G. Hydraulic fracturing in a sedimentary geothermal reservoir: Results and implications. *International Journal of Rock Mechanics and Mining Sciences*. 2005;42(7-8):1028-1041.
55. Liu X, Zhang Z, Ge Z, Zhong C, Liu L. Brittleness Evaluation of Saturated Coal Based on Energy Method from Stress–Strain Curves of Uniaxial Compression. *Rock Mechanics and Rock Engineering*. 2021:1-15.
56. Lu Y, Li Y, Wu Y, Luo S, Jin Y, Zhang G. Characterization of shale softening by large volume-based nanoindentation. *Rock Mechanics and Rock Engineering*. 2020;53(3):1393-1409.
57. Pirzada M, Roshan H, Sun H, et al. Effect of contact surface area on frictional behaviour of dry and saturated rock joints. *Journal of Structural Geology*. 2020;135:104044.
58. Iqbal MA, Rezaee R, Laukamp C, Pejčić B, Smith G. Integrated sedimentary and high-resolution mineralogical characterisation of Ordovician shale from Canning Basin, Western Australia: Implications for facies heterogeneity evaluation. *Journal of Petroleum Science and Engineering*. 2022;208:109347.
59. Luan X, Di B, Wei J, Zhao J, Li X. Creation of synthetic samples for physical modelling of natural shale. *Geophysical Prospecting*. 2016;64(4):898-914.
60. Rezaee R. *Fundamentals of gas shale reservoirs*. John Wiley & Sons; 2015.
61. Zeng L, Reid N, Lu Y, Hossain MM, Saedi A, Xie Q. Effect of the fluid–shale interaction on salinity: implications for high-salinity flowback water during hydraulic fracturing in shales. *Energy & Fuels*. 2020;34(3):3031-3040.
62. De Pater C, Cleary M, Quinn T, Barr D, Johnson D, Weijers L. Experimental verification of dimensional analysis for hydraulic fracturing. *SPE Production & Facilities*. 1994;9(04):230-238.
63. Bura E, Seweryn A. Mode I fracture in PMMA specimens with notches—Experimental and numerical studies. *Theoretical and Applied Fracture Mechanics*. 2018;97:140-155.
64. Long R, Hui C-Y, Gong JP, Bouchbinder E. The fracture of highly deformable soft materials: A tale of two length scales. *Annual Review of Condensed Matter Physics*. 2020;12
65. Wang H, Dyskin A, Pasternak E, Dight P. 3D crack growth in biaxial compression: influence of shape and inclination of initial cracks. *Rock Mechanics and Rock Engineering*. 2020;53(7):3161-3183.
66. Zhou D, Zhang G, Zhao P, Wang Y, Xu S. Effects of post-instability induced by supercritical CO₂ phase change on fracture dynamic propagation. *Journal of Petroleum Science and Engineering*. 2018;162:358-366.
67. Han D-h, Nur A, Morgan D. Effects of porosity and clay content on wave velocities in sandstones. *Geophysics*. 1986;51(11):2093-2107.
68. Li JX, Rezaee R, Müller TM, Sarmadivaleh M. Pore Size Distribution Controls Dynamic Permeability. *Geophysical Research Letters*. 2021;48(5):e2020GL090558.